COMPUTER PROCESSING AND MODELING – Full Paper

Magnetic Resonance in Medicine 79:2804–2815 (2018)

Joint Arterial Input Function and Tracer Kinetic Parameter Estimation from Undersampled Dynamic Contrast-Enhanced MRI Using a Model Consistency Constraint

Yi Guo,[1]* Sajan Goud Lingala,[1] Yannick Bliesener,[1] R. Marc Lebel,[2] Yinghua Zhu,[1] and Krishna S. Nayak[1]

Purpose: To develop and evaluate a model-based reconstruction framework for joint arterial input function (AIF) and kinetic parameter estimation from undersampled brain tumor dynamic contrast-enhanced MRI (DCE-MRI) data.

Methods: The proposed method poses the tracer-kinetic (TK) model as a model consistency constraint, enabling the flexible inclusion of different TK models and TK solvers, and the joint estimation of the AIF. The proposed method is evaluated using an anatomic realistic digital reference object (DRO), and nine retrospectively down-sampled brain tumor DCE-MRI datasets. We also demonstrate application to 30-fold prospectively undersampled brain tumor DCE-MRI.

Results: In DRO studies with up to 60-fold undersampling, the proposed method provided TK maps with low error that were comparable to fully sampled data and were demonstrated to be compatible with a third-party TK solver. In retrospective undersampling studies, this method provided patient-specific AIF with normalized root mean-squared-error (normalized by the 90th percentile value) less than 8% at up to 100-fold undersampling. In the 30-fold undersampled prospective study, the proposed method provided high-resolution whole-brain TK maps and patient-specific AIF.

Conclusion: The proposed model-based DCE-MRI reconstruction enables the use of different TK solvers with a model consistency constraint and enables joint estimation of patient-specific AIF. TK maps and patient-specific AIF with high fidelity can be reconstructed at up to 100-fold undersampling in k,t-space. **Magn Reson Med 79:2804–2815, 2018. © 2017 International Society for Magnetic Resonance in Medicine.**

Key words: model-based reconstruction; compressed sensing; DCE-MRI; kinetic modeling

INTRODUCTION

Dynamic contrast-enhanced (DCE) MRI is a powerful technique for probing subvoxel vascular properties of tissue including fractional plasma volume, fractional extracellular–extravascular volume, and clinically important transfer constants. DCE-MRI involves capturing a series of images before, during, and after administration of a T_1-shortening contrast agent. Tracer-kinetic (TK) parameter maps are then computed from the dynamic images, and provide information for diagnosis and monitoring treatment response (1–3). DCE-MRI is used throughout the body, most commonly in the prostate, breast, liver, and brain. In the brain, DCE-MRI has shown value in the assessment of brain tumor, multiple sclerosis, and Alzheimer disease (4–6).

With conventional Nyquist sampling, DCE-MRI is often unable to simultaneously provide adequate spatio-temporal resolution and spatial coverage. A typical brain DCE-MRI provides 5-s temporal resolution, which is a minimum requirement for accurate TK modeling (7,8). Using Cartesian sampling at the Nyquist rate, only 5–10 slices are achievable. This is typically inadequate in large glioblastoma cases and cases with scattered metastatic disease that may be spread throughout the brain (9). It is possible to coarsen spatial resolution to achieve greater spatial coverage, but this compromises the ability to evaluate the narrow (1–2 mm) enhancing margin of glioblastomas and the ability to evaluate small lesions.

Thus, techniques involving undersampling and constrained reconstruction have been proposed to simultaneously provide high spatial resolution and whole-brain coverage. Early work used compressed sensing and parallel imaging to reconstruct dynamic images from undersampled k,t-space data (10–12). Standard TK modeling software was then used to generate high-resolution whole-brain TK maps based on the reconstructed images (9,13). A more recent proposed approach was to enforce

[1]Ming Hsieh Department of Electrical Engineering, Viterbi School of Engineering, University of Southern California, Los Angeles, California, USA.

[2]GE Healthcare, Calgary, Canada.

Grant sponsor: National Center for Advancing Translational Sciences of the National Institutes of Health; Award number: UL1TR000130 (formerly National Center for Research Resources; Award Number UL1RR031986); Grant sponsor: National Institutes of Health; Award Number 5UL1TR000130-04.

The content of this article is solely the responsibility of the authors and does not necessarily represent the official views of the National Institutes of Health.

*Correspondence to: Yi Guo, Ph.D., Ming Hsieh Department of Electrical Engineering, Viterbi School of Engineering, University of Southern California, 3740 McClintock Avenue, EEB 400, Los Angeles, CA, 90089-2564. E-mail: yiguo@usc.edu; Twitter: @Eagle13GY

Correction added after online publication 13 October 2017. The authors updated the title to correct "Tracker" to "Tracer."

Received 13 April 2017; revised 11 August 2017; accepted 16 August 2017

DOI 10.1002/mrm.26904

Published online 14 September 2017 in Wiley Online Library (wileyonlinelibrary.com).

the TK model and directly estimate TK parameters from undersampled k,t-space data (14). Similar model-based reconstruction approaches have been used for MRI relaxometry (15,16), PET kinetic parameter estimation (17,18), and recently, DCE-MRI kinetic parameter estimation (14,19–21). Compared with conventional compressed sensing techniques that reconstruct dynamic images first, the model-based approach provides superior results and allows higher undersampling rates (14,21). Direct kinetic parameter estimation makes the most efficient use of acquired information; however, it is sensitive to inaccuracy of the forward model. Two major issues with this are variations in the arterial input function (22) and prior knowledge of the appropriate TK model (23–25).

In conventional DCE-MRI, images are reconstructed for each time point. Patient-specific arterial input functions (AIF) can be identified from vessel pixels using either manual region of interest (ROI) selection or automatic cluster-based ROI selection (26). Some centers use a fixed population-averaged AIF (27), an institutionally derived population AIF, or a delay and dispersion-corrected version of these (9). The use of a patient-specific AIF (pat-AIF) is generally preferred because it is known to provide more accurate TK mapping (22). The estimation of pat-AIF from undersampled data is extremely challenging due to undersampling artifacts. Current model-based TK reconstruction approaches rely on the use of a population-averaged AIF (pop-AIF) (14,21). This is considered a major limitation of these approaches because the use of a pop-AIF can lead to significant errors in the resulting TK maps (22).

In this study, we developed a DCE-MRI reconstruction approach that allows for integration of different TK models and/or different TK solvers as well as joint estimation of the patient-specific AIF and TK parameter maps. We evaluated the performance of the proposed method using simulated DCE-MRI data from a physiologically realistic digital reference object (DRO) and in vivo DCE-MRI data from brain tumor patients. We also tested its application to prospectively undersampled high-resolution whole-brain DCE-MRI data.

We propose simultaneous reconstruction of TK maps and dynamic images, where TK model consistency is applied as a penalized reconstruction constraint and the pat-AIF can be iteratively estimated from the dynamic images. This approach is inspired by recent studies of accelerated quantitative MR relaxometry (28,29), where physical or physiological model consistency was applied as a penalized reconstruction constraint (not strictly enforced). This consistency constraint allowed for the data fit to deviate from the model, which made the scheme robust to scenarios with model inconsistencies (e.g., motion). For DCE-MRI, TK model is applied as a consistency constraint with a regularization parameter that balances the tradeoff between data consistency and model consistency. We show that this approach provides a much more flexible framework for direct model-based reconstruction of accelerated DCE-MRI.

THEORY

Model Consistency Constraint

This method jointly estimates contrast concentration versus time images (C) and TK parameter maps (θ) from the undersampled data (y) by solving the following least-squares problem:

$$(C,\theta) = \underset{C,\theta}{\operatorname{argmin}} ||UFE(\psi C + S_0) - y||_2^2 + \beta||P(\theta) - C||_2^2. \quad [1]$$

The first l_2 norm represents data consistency, where C should be consistent with the measured data y by Ψ (signal equation), U (undersampling mask), F (Fourier transform), and E (sensitivity encoding). S_0 is the first temporal frame images that are fully sampled. The second l_2 norm represents model consistency, where C is consistent to the forward modeling (P) of TK parameter maps (Patlak, eTofts etc.). This formulation can be simplified to

$$(C,\theta) = \underset{C,\theta}{\operatorname{argmin}} ||AC - b||_2^2 + \beta||P(\theta) - C||_2^2, \quad [2]$$

where $A = UFE\Psi$ represents data consistency modeling, $b = (y + UFES_0)$ is the known data.

To solve the least-square optimization problem in Equation [2], we alternatively solve for each variable while keeping others constant. For each iteration n,

$$C^{n+1} = \underset{C}{\operatorname{argmin}} ||AC - b||_2^2 + \beta||P(\theta^n) - C||_2^2, \quad [3]$$

$$\theta^{n+1} = P^{-1}(C^{n+1}). \quad [4]$$

Note that Equation [3] is regularized SENSE reconstruction with an l_2 norm constraint that can be solved efficiently using conjugate gradients (30). Equation [4] is backward TK modeling that can be solved using any DCE-MRI modeling toolbox. Because forward modeling (P) and backward modeling (P^{-1}) are used iteratively, the modeling solver should not utilize linearization or other forms of approximation. For example, ROCKETSHIP (31) and TOPPCAT (32) are two suitable solvers. Detailed substeps and variants of Equations [3] and [4] are provided in the Appendix.

Joint AIF and TK Parameter Estimation

The proposed formulation allows for joint estimation of the patient-specific AIF. Equation [2] can be modified to estimate C, θ, and AIF from undersampled data by solving the following least-squares problem:

$$(C,\theta,AIF) = \underset{C,\theta,AIF}{\operatorname{argmin}} ||AC - b||_2^2 + \beta||P(\theta,AIF) - C||_2^2. \quad [5]$$

Similar to the above, we solve each variable alternatively as follows (n^{th} iteration):

$$C^{n+1} = \underset{C}{\operatorname{argmin}} ||AC - b||_2^2 + \beta||P(\theta^n,AIF) - C||_2^2 \quad [6]$$

$$\theta^{n+1}, AIF^n = P^{-1}(C^{n+1}). \quad [7]$$

Equation [7] is backward TK modeling from contrast concentration including pat-AIF estimation. This can be performed by identifying an arterial ROI once, using the time-averaged image or postcontrast image. Within each iteration, it is then possible to: 1) apply this ROI to C to estimate the AIF (averaging the pixels) and 2) use the updated AIF during TK modeling. This is a common procedure in TK modeling for DCE-MRI. The only difference is

identification of the arterial ROI before the reconstruction of the dynamic images.

Theoretical Benefits

The proposed method formulates model consistency as a constraint with a penalty β and decouples it from data consistency. There are multiple benefits of this formulation: 1) algorithm complexity is reduced compared to recently proposed direct reconstruction techniques that require complex cost function gradient evaluations (14,20,33); 2) different TK models can easily be included in this formulation, as described above; 3) patient-specific AIFs can be estimated jointly with TK maps, as described above; and 4) the penalty β can allow for TK model deviation, reducing errors that may be caused by strict model enforcement (29). This study specifically demonstrates items #2 and #3.

METHODS

Data Sources

Digital Reference Object

Anatomically realistic brain tumor DCE-MRI DRO was generated based on the method and data provided by Bosca and Jackson (34). The extended Tofts (eTofts) model was used to generate contrast concentration curves with known TK parameter maps and pop-AIF (27). Coil sensitivity maps measured on our MRI scanner (3T, eight-channel head coil) were coregistered to the DRO and used to generate realistic MRI k-space data (35). Gaussian noise were added to the image space to simulate noise levels typical of DCE-MRI at 3T and 1.5T.

Retrospective

Nine anonymized fully sampled brain tumor DCE-MRI raw data sets were obtained from patients who had undergone routine brain MRI examinations with contrast (including DCE-MRI) at our institution. The study protocol was approved by our Institutional Review Board. The acquisition was based on a 3D Cartesian fast spoiled gradient echo (SPGR) sequence using the following parameters: field of view $= 22 \times 22 \times 4.2\,cm^3$, spatial resolution $= 0.9 \times 1.3 \times 7.0\,mm^3$, temporal resolution $= 5$ s, 50 time frames, eight receiver coils, flip angle $= 15^\circ$, echo time $= 1.3$ ms, repetition time $= 6$ ms. DESPOT1 was performed before DCE-MRI, with a flip angle of 2°, 5°, and 10° to estimate precontrast T_1 and M0 maps. The contrast agent, gadobenate dimeglumine [MultiHance Bracco Inc.; relaxivity $r_1 = 4.39\ s^{-1} \cdot mM^{-1}$ at 37°C at 3T (36)] was administered with a dose of 0.05 mmol/kg, followed by a 20-mL saline flush in the left arm via intravenous injection.

Prospective

Prospectively undersampled data were acquired in one brain tumor patient (male, age 65 years, glioblastoma) with Cartesian golden-angle radial k-space sampling (9,37). 3D SPGR data were acquired continuously for 5 min. Whole-brain coverage was achieved with a field of view of $22*22*20\,cm^3$ and spatial resolution of $0.9*0.9*1.9\,mm^3$. The prospective study protocol was approved by our Institutional Review Board. Written informed consent was provided by the participant.

Demonstration of TK Solver Flexibility

To demonstrate TK solver flexibility, DRO data was retrospectively undersampled using a randomized golden-angle sampling pattern at $R = 60\times$ (37). Gaussian noise were added to the image space, creating signal-to-noise ratio (SNR) levels of 20 and 10 (white matter based) for simulation of DCE-MRI image quality at 3T and 1.5T. The proposed method with eTofts modeling was used to reconstruct TK parameter maps at $R = 60\times$ and SNR $= 20$ and 10, respectively. An in-house gradient-based algorithm and an open-source TK modeling toolbox, ROCKETSHIP (31), were used for the eTofts solver in the proposed algorithm (Eq. [4]). Tumor ROI K^{trans} correlation coefficient, R^2 and normalized root mean-squared-error (nRMSE, normalized by the 90th percentile value within the tumor ROI) between the estimated and true values were calculated and compared. Note that tumor ROI 90th percentile K^{trans} value has been found to be a sensitive and clinically valuable DCE-MRI biomarker (38,39), hence normalization of RMSE by this value. TK maps estimated from the noisy fully sampled images (SNR $= 20$, $R = 1\times$) were also compared with the true TK maps to evaluate the performance of the proposed method with respect to errors found in conventional DCE-MRI.

Demonstration of TK Model Flexibility

The nine fully sampled patient data were fitted to the Patlak and eTofts models to calculate the model fitting error, and an F-test was performed in the tumor ROI to determine whether the Patlak or eTofts model is the most appropriate fit (23–25). In the F-test (40,41), the null hypothesis is that the two samples of sum-of-squared modeling errors were drawn from the same pool. The failure of this hypothesis leads to acceptance of the higher-order model. Thus, for each pixel, the F-test will reveal whether a higher-order model (eTofts model) should be used (23–25). If more than 50% of the tumor pixels were appropriately fitted for a certain model, this model was selected for the data set. We reconstructed the corresponding TK parameter maps for fully sampled data (used as reference) and at undersampling rates of $20\times$, $60\times$, and $100\times$ for all nine cases. A randomized golden-angle sampling pattern (37) was used in the k_x-k_y plane, simulating k_y-k_z phase encoding in a 3D whole-brain acquisition. Images were reconstructed using a pop-AIF (27) with patient-specific delay corrected by the delay estimated from k-space center (42). ROI-based K^{trans} nRMSE and K^{trans} histograms were calculated based on the reference K^{trans} maps. K^{trans} histogram skewness and 90th percentile K^{trans} values were also measured for evaluation, as they have been shown to be valuable in the clinical assessment of brain tumors by DCE-MRI (38,39,43).

Demonstration of Joint AIF and TK Estimation

The cases following the Patlak model were reviewed with special attention to vessel signal. Cases that showed significant precontrast inflow enhancement were

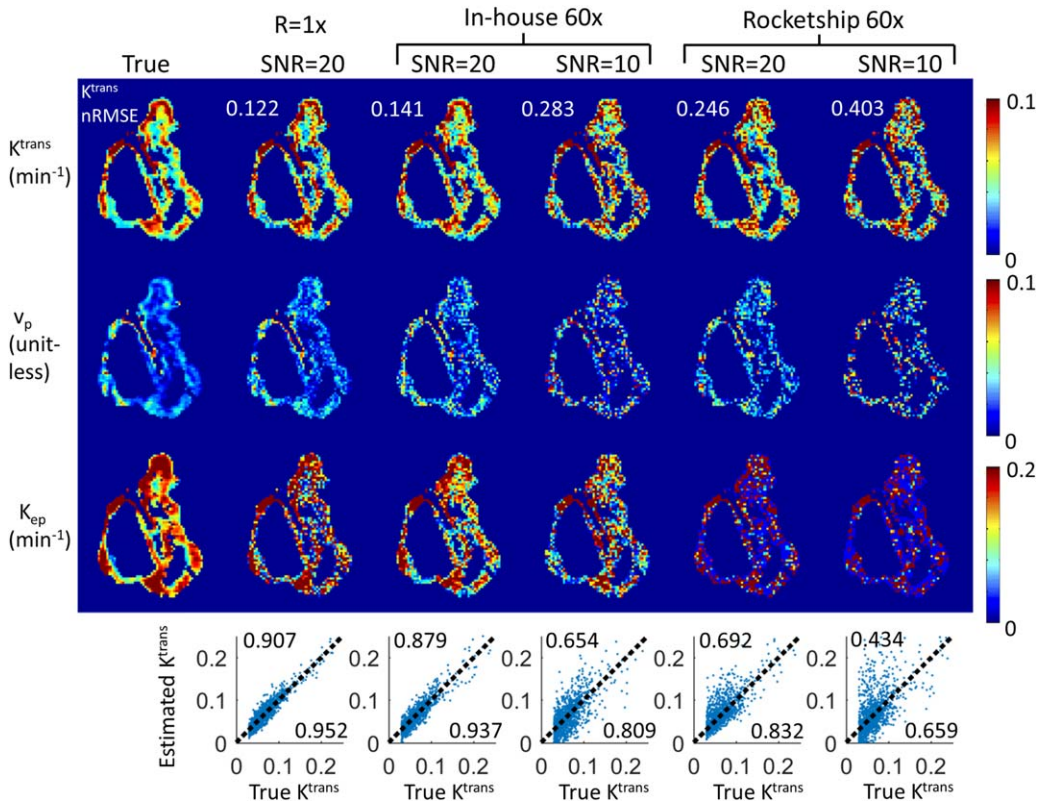

FIG. 1. The proposed method is compatible with third-party TK solvers. Shown are results from an anatomically realistic brain-tumor DCE-MRI digital reference object using an in-house solver and the ROCKETSHIP solver, both using the model consistency constraint method. $R = 60\times$ were tested at white matter SNR level of 20 and 10. Tumor ROI K^{trans} nRMSE (normalized to 90th percentile value) were shown on the upper left corner of respective K^{trans} maps. Correlation plots are shown at the bottom of each respective result, where the upper left corner shows the R^2 value and the lower right corner shows the correlation coefficient. Both methods were able to restore K^{trans} maps with less than 50% nRMSE, whereas the ROCKETSHIP solver yielded K^{trans} maps with higher errors, especially at SNR = 10. K_{ep} and v_p maps are more sensitive to noise, especially when using the ROCKETSHIP solver.

identified and subsequently excluded. With the remaining cases, we performed joint estimation of AIF and Patlak parameter maps from undersampled data across sampling rates of 20×, 60×, and 100×. For each undersampling rate, 15 realizations were generated by varying the initial angle of the golden-angle radial sampling pattern (37). The golden-angle radial sampling with different initial angle will create mostly nonoverlapped k-space coverage, effectively providing different noise realizations with the same noise level (white matter SNR = 20). Reconstructed patient-specific AIFs were compared with the fully sampled reference using nRMSE (normalized to the 90th percentile AIF value over time) and bolus peak difference. ROI-based K^{trans} nRMSE (normalized to the 90th percentile K^{trans} value over the tumor ROI) were also calculated for evaluation.

Demonstration with Prospectively Undersampled Data

We tested the application of the proposed method for joint AIF and TK parameter estimation on prospectively $30\times$ undersampled high-resolution whole-brain DCE-MRI data. Five-second temporal resolution was achieved by grouping raw (k,t)-space data acquired within consecutive 5-s intervals, effectively $30\times$ undersampling compared with Nyquist sampling (44). pat-AIF and TK maps were jointly reconstructed using the proposed model consistency constraint approach. pat-AIF ROI was selected based on time-averaged images. Three-plane of K^{trans} and v_p maps and pat-AIF are presented for visual assessment.

RESULTS

Figure 1 shows the DRO reconstruction results at $R = 60\times$ for SNR = 20 and 10. The eTofts model was used to generate the simulated DCE-MRI data, and also for model-based reconstruction. TK maps estimated from fully sampled ($R = 1\times$) noisy images are also shown to evaluate the performance in the context of normal DCE-MRI modeling with noise. $\beta = 0.1$ and iteration = 100 were chosen based on prior experiments. Computation time for the conversion from concentration versus time to TK maps was 3.44 s for the in-house gradient-based method, and 31.62 s for ROCKETSHIP with parallel computing turned on (four workers). Pixel-wise correlation plots between the true and estimated K^{trans} values are shown at the bottom row, with calculated R^2 at the upper left corner, and correlation coefficient at the lower right corner. Both methods were able to restore K^{trans} maps with less than 50% error, and the in-house solver was able to restore the TK maps at the quality close to fully sampled noisy results. The ROCKETSHIP solver is

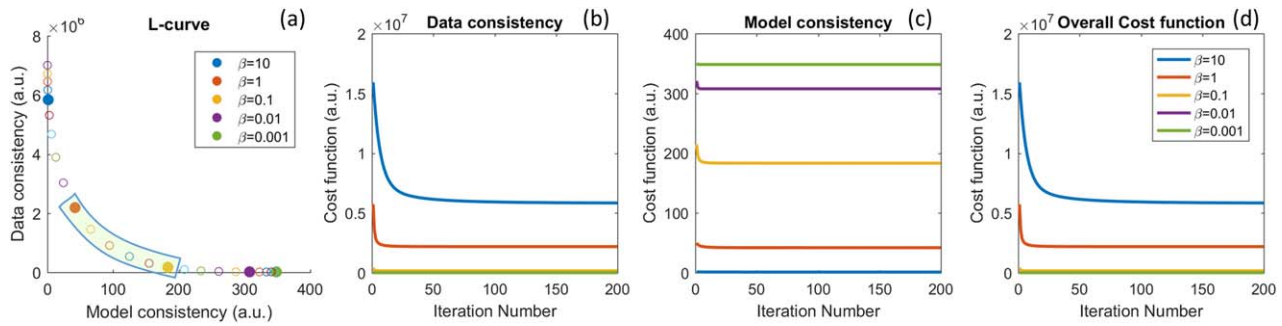

FIG. 2. Performance for different β values at R = 20 × for one representative in vivo data set. (**a**) The l-curve shows that β value controls the balance between model and data consistency. (**b–d**) Convergence of the cost function to within 1% of its final value required 116, 24, 10, 4, and 2 iterations for β values of 10, 1, 0.1, 0.01, and 0.001, respectively. The actual reconstructed TK maps for different β values are shown in Figure 3.

more sensitive to increased noise level, especially for K_{ep} and v_p maps. These results show that the proposed method can restore TK maps from highly undersampled data (R = 60×) with quality close to modeling results from fully sampled noisy images. It also shows that this method is compatible with a third-party TK solver.

Figures 2 and 3 illustrate the impact of regularization parameter β for one representative in vivo brain tumor dataset, using the Patlak model, at R = 20×. The cost function values as a function of iteration number, l-curve, and the final reconstructed TK maps are plotted for different β values. A large β resulted in slow convergence, whereas a smaller β provided fast convergence. This behavior was expected, as ill-conditioning of the problem in Equation [3] increases with β (45). TK maps obtained with a large β showed poor fidelity as data consistency was violated, whereas the maps with a small β were equivalent to a SENSE reconstruction without constraints and demonstrated g-factor–related artifacts at R = 20×. The L-curve shows the balance between the data consistency and model consistency, based on which of the β values in the range of 0.1 to 1 (green highlighted) show similar performance. We then tuned the β value in this range for different cases. We found the acceptable range to be roughly 1 order of magnitude and to be consistent among the four cases that we examined carefully.

Based on the tumor ROI F-test, the Patlak model was appropriate for six in vivo cases, whereas the e-Tofts model was appropriate for three in vivo cases. Figures 4 and 5 show representative cases of Patlak and eTofts model, respectively, at R = 60 × and R = 100×. K^{trans} and v_p maps on the zoomed-in tumor region are shown (K_{ep} for eTofts is not shown). Histograms of the K^{trans} values within the tumor ROI are plotted for the respective cases (bottom row). Figure 6 shows quantitative evaluation of all the in vivo reconstruction results focusing on K^{trans} values. For Patlak model reconstruction, the 90the percentile K^{trans} values matched well with the reference values across all cases and, the histogram skewness was also reasonably matched. Across all cases and undersampling rates, nRMSE was less than 32%. For the eTofts model, the 90th percentile K^{trans} values matched well with reference for one case and had larger deviation for

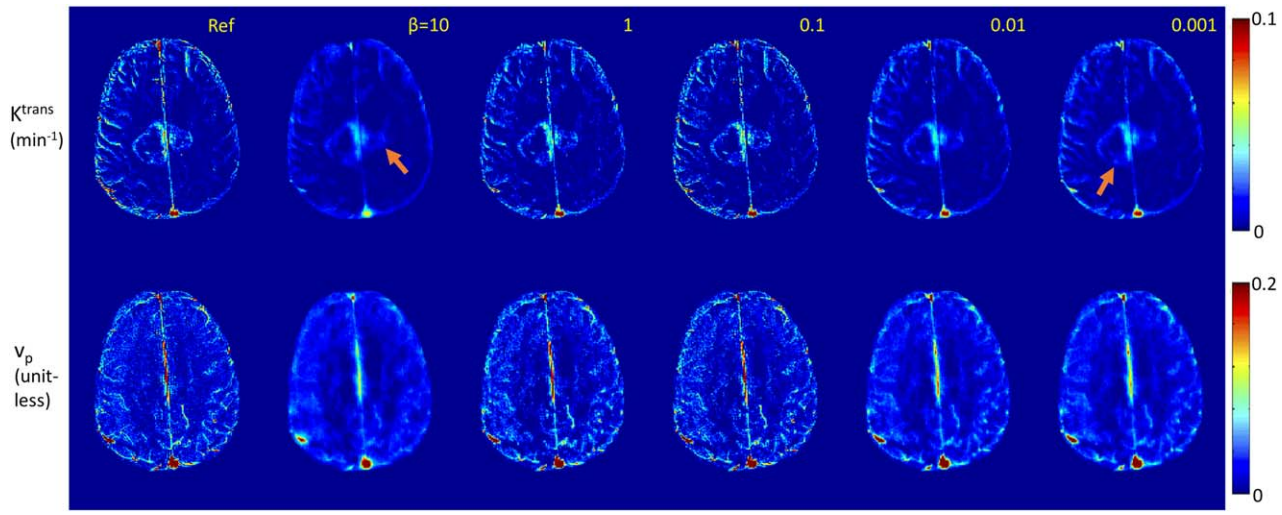

FIG. 3. TK maps reconstructed for different β values using the case described in Figure 2. Tumor ROI nRMSE (K^{trans}) are 0.102, 0.073, 0.072, 0.098, and 0.105 for β values 10, 1, 0.1, 0.01, and 0.001, respectively. Reconstruction with small β values converged quickly and is closer to a SENSE reconstruction with associated g-factor losses and undersampling artifacts. Reconstruction with large β values shows slow convergence and provides less accurate TK maps due to the data consistency being violated.

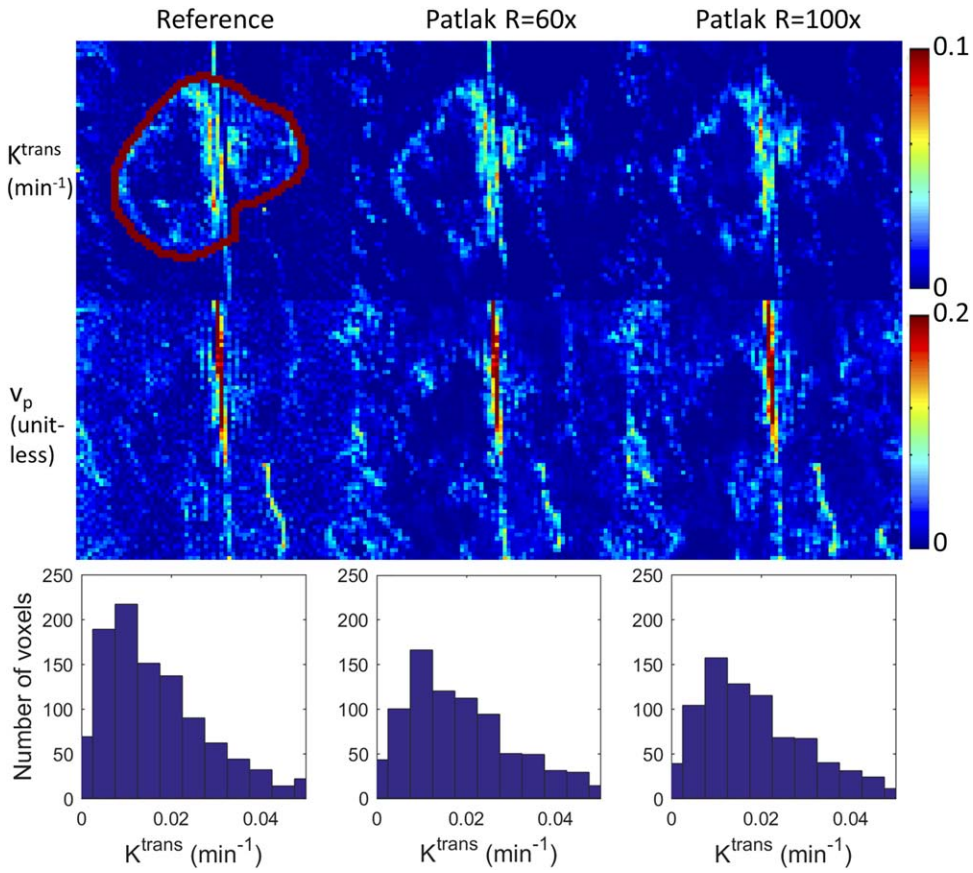

FIG. 4. Reconstruction of the TK maps of one representative in vivo brain tumor case using the Patlak model at $R = 60\times$ and $100\times$. Tumor ROI (indicated in the reference images) histograms are shown below the respective cases. Detailed evaluation of the ROI K^{trans} histograms by skewness, 90th percentile, and nRMSE are shown in Figure 6.

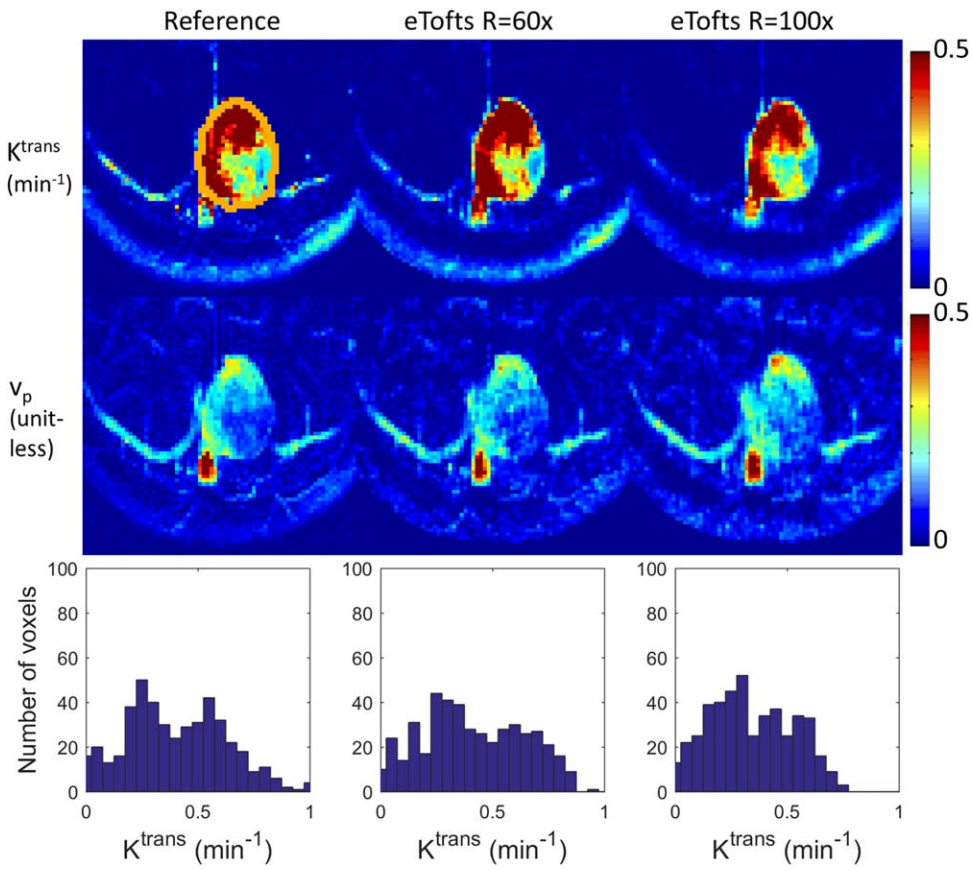

FIG. 5. Reconstruction of the TK maps of one representative in vivo brain tumor case using the eTofts model at $R = 60\times$ and $100\times$. Tumor ROI (indicated in the reference images) histograms are shown below the respective cases. Detailed evaluation of the ROI K^{trans} histograms by skewness, 90th percentile, and nRMSE are shown in Figure 6.

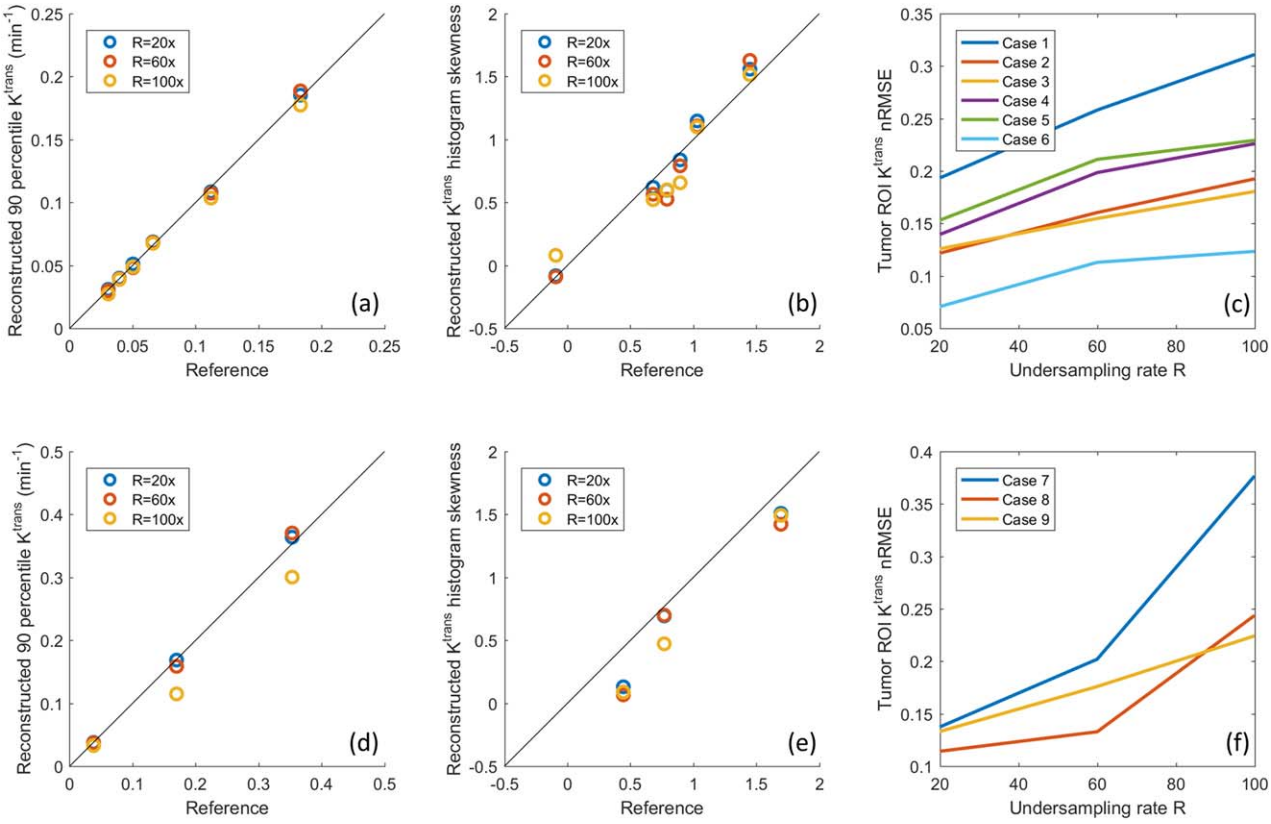

FIG. 6. Quantitative evaluation of Patlak (top row) and eTofts (bottom row) reconstruction on nine retrospective undersampled in vivo cases. The 90th percentile of the reconstructed K^{trans} values for different cases was plotted against the reference 90th percentile K^{trans}. (**a**) For the Patlak model, the values matched well for all cases and undersampling rates. (**d**) For the eTofts model, the values matched well for $R = 20\times$ and $60\times$ and had larger deviation for $R = 100\times$. (**b, e**) The K^{trans} histogram skewness was also plotted against the reference histogram skewness. The tumor ROI K^{trans} nRMSE (normalized based on reference 90th percentile K^{trans} value) were plotted against different R's across different cases. (**c**) For Patlak reconstruction, the nRMSE were less than 32% consistently for all cases and undersampling factors. (**f**) For eTofts reconstruction, the nRMSE were less than 15% at lower undersampling rates, then increase considerably at higher undersampling rates.

the other cases at $R = 100\times$. The nRMSE also increased considerably as the undersampling rate was increased.

Figure 7 shows the selection of AIF ROI from undersampled data, the comparison of pop-AIF and pat-AIF, and the resulting TK maps in one representative in vivo data set. This figure shows that the ROI of pat-AIF can be easily selected based on average of undersampled data. This ROI can then be used for joint reconstruction of AIF and TK parameters in the proposed method. Figure 8 shows the reconstruction results of TK maps and pat-AIF (same case as Fig. 7) at different undersampling rates. Compared with the AIF extracted from fully sampled data, the proposed method was able to provide clear depiction of AIF peak up to $R = 100\times$, with good-quality TK maps restored at the same time.

Figure 9 shows the quantitative evaluation of joint AIF and TK reconstruction across the four in vivo data sets. Based on the nRMSE of the TK maps, TK maps can be restored with error less than 30% at for all cases and undersampling rates. Radial sampling patterns with different initial angle created different noise realization for each case, and multiple noise realizations show that the method is robust to noise, with an expected increase in variance at higher undersampling rates. The shape of the AIF can be estimated at up to $R = 100\times$, with AIF nRMSE below 8% for all cases. The peak of the AIF shows larger variance for different noise realization, since the peak is only one point. However, the proposed method is still able to restore the AIF peak up to $R = 60\times$, with the error at most 0.25 mmol across all cases.

Figure 10 shows reconstruction of pat-AIF and TK maps from prospectively undersampled in vivo data from a brain tumor patient. This result demonstrates that whole-brain TK maps can be reconstructed jointly with patient-specific AIF, with no obvious undersampling artifacts in the final TK maps. The clinically meaningful benefits of undersampling can be best demonstrated in a prospective study, where arbitrary reformats of the 3D TK maps are made possible by the ability to achieve high spatial resolution and whole-brain coverage.

DISCUSSION

We have described, demonstrated, and evaluated a novel model-based reconstruction approach for DCE-MRI in which the TK model is posed as a penalized consistency constraint. By this formulation, we decoupled the TK

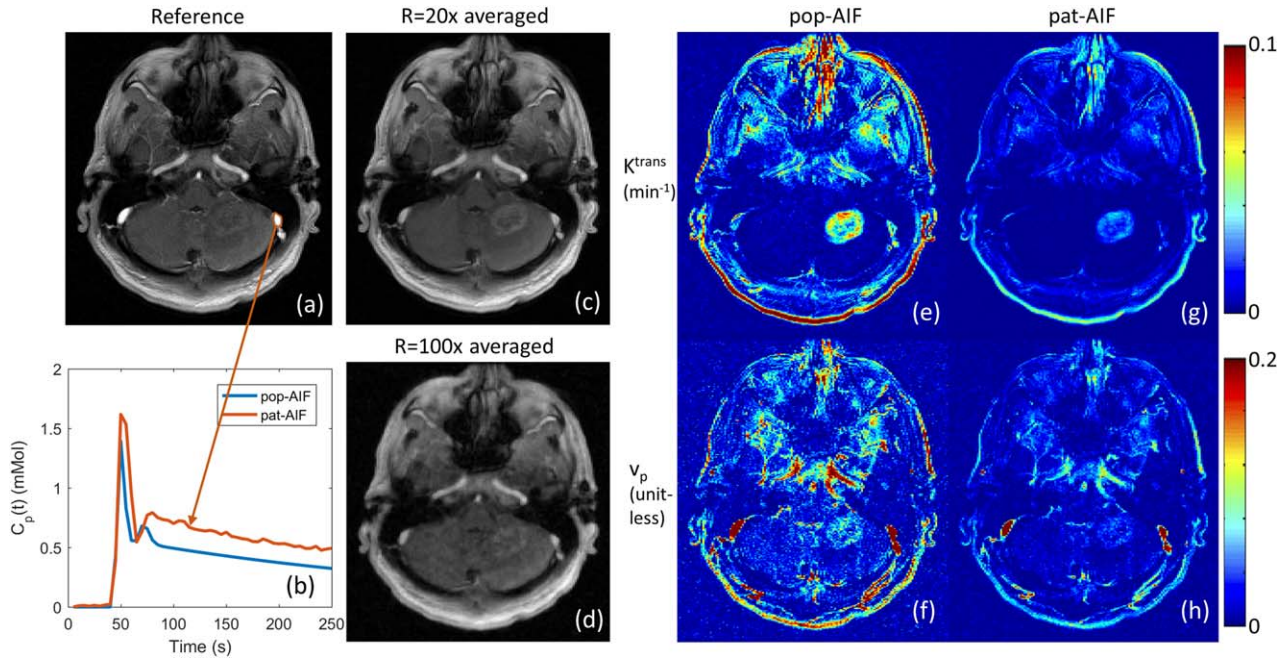

FIG. 7. Left: Extraction of pat-AIF (**b**) from a manually selected ROI on the peak contrast frame of fully sampled in vivo data set (**a**). The pop-AIF shown in panel b was delay corrected. In the undersampling scenario, a time-averaged image can be generated (**c**), and even at R = 100 × (**d**) it is straightforward to select an artery ROI from this image for the joint AIF and TK map reconstruction. Right: Different AIFs can result in different TK maps (**e**–**h**), and pat-AIF is preferred for more accurate TK modeling.

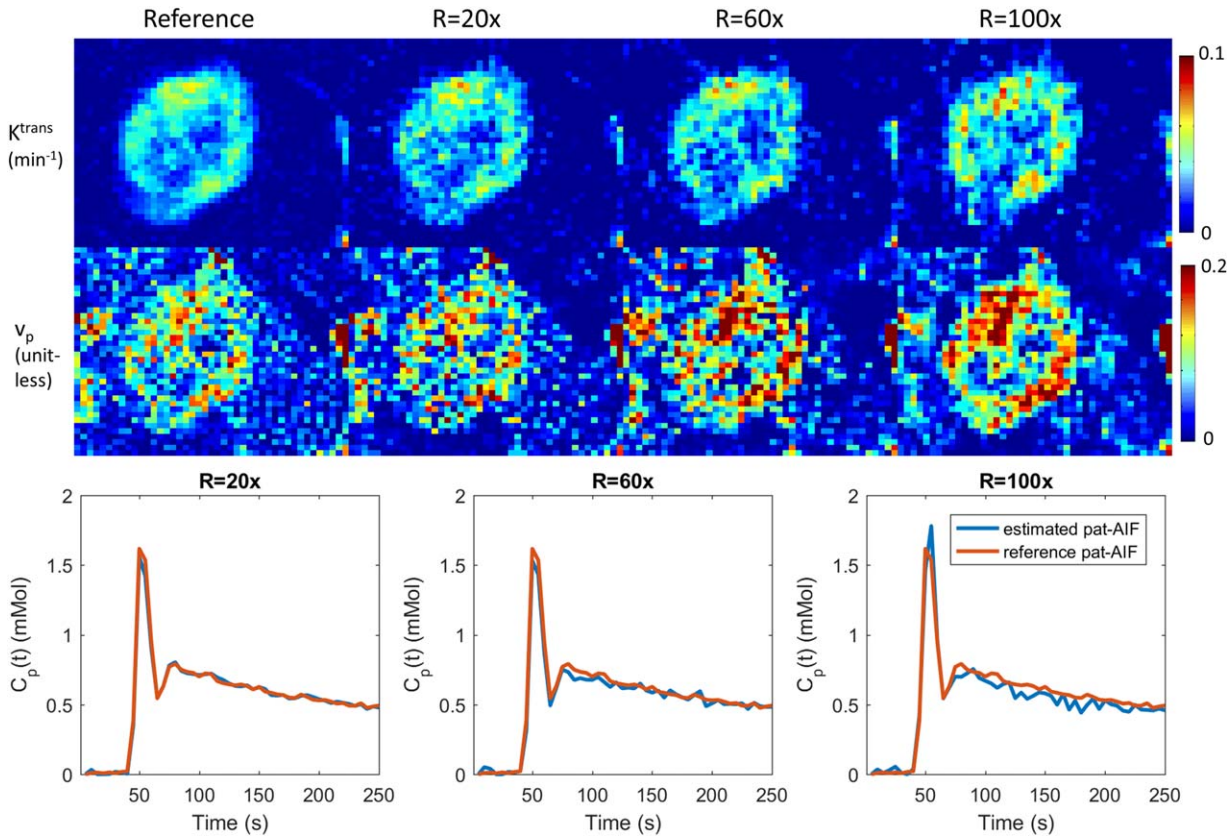

FIG. 8. Joint reconstruction of TK maps (cropped portion of the case in Fig. 5) and AIF at R = 20×, 60×, and 100 × for one representative in vivo case. Compared with the fully sampled reference, the proposed method is able to restore both AIF and TK maps at the same time, even at a high undersampling rate of 100×. Quantitative evaluation of TK maps and AIF, including this case, are presented in Figure 7. Supporting Video S1 demonstrates the estimated pat-AIF versus iteration number.

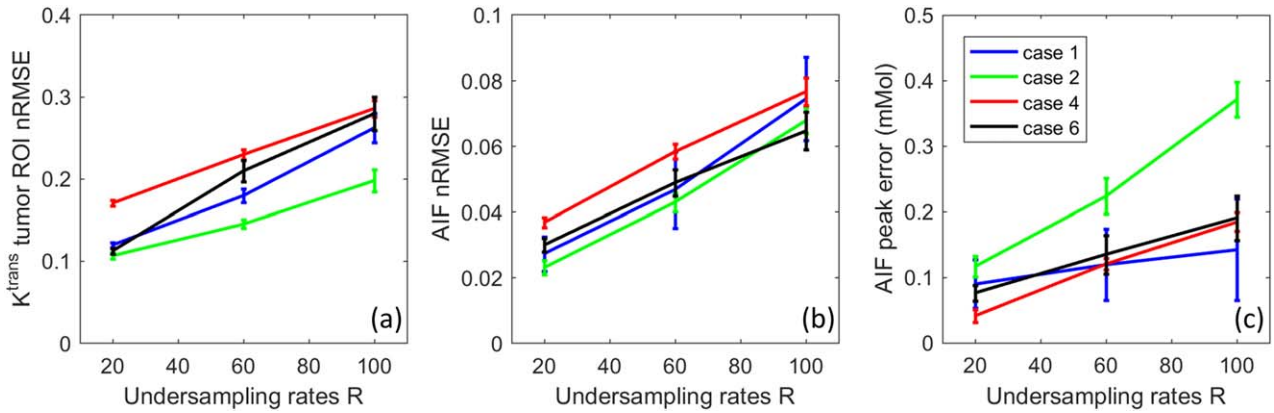

FIG. 9. Quantitative evaluation of the joint AIF and TK reconstruction for the four in vivo retrospective undersampled cases across R = 20×, 60×, and 100×. (**a**) K^{trans} nRMSE was calculated as the spatial RMSE across all tumor pixels, divided by the 90th percentile of the reference tumor K^{trans} value. (**b**) AIF nRMSE was calculated as the temporal RMSE divided by the 90th percentile of the reference AIF. (**c**) AIF peak error was calculated as the reference peak minus the estimated peak. As expected, the nRMSE mean and variance all increased with undersampling rate across different cases.

model consistency from the k,t space data consistency. The two sub-problems can be solved using existing techniques, namely TK modeling (including AIF estimation) and regularized SENSE reconstruction. The proposed approach allows for easy inclusion of different TK solvers, including third-party solvers, and also allows for joint estimation of the patient-specific AIF. We have demonstrated the robustness of the proposed method in one anatomically realistic brain tumor DRO, and a retrospective study of nine brain tumor DCE-MRI datasets. The DRO study demonstrated that the proposed method provides performance comparable to conventional TK modeling results from fully sampled noisy images, with only a 2% higher error at 60-fold undersampling. The retrospective study shows that the proposed method is robust to noise across different cases, and can provide accurate TK maps with less than 32% error, and AIF with less than 8% error up to 100-fold undersampling. We also demonstrated the application of the proposed method to prospectively undersampled data, where whole-brain high-resolution TK maps can be jointly reconstructed with pat-AIF.

The proposed method has a few important limitations. First, the alternating algorithm proposed is a two-loop iteration, where an iterative solver is needed for each subproblem. Compared with a gradient-based direct reconstruction (14), this formulation takes longer computing time. This issue can be addressed by using more powerful computers, implementing in C, and/or using GPU acceleration.

Second, although we demonstrate that the proposed method is compatible with a third-party solver, it requires that the solver not use any approximation for the modeling. This is because the proposed approach requires the backward and forward modeling operators to be exact inverses of each other, otherwise error will

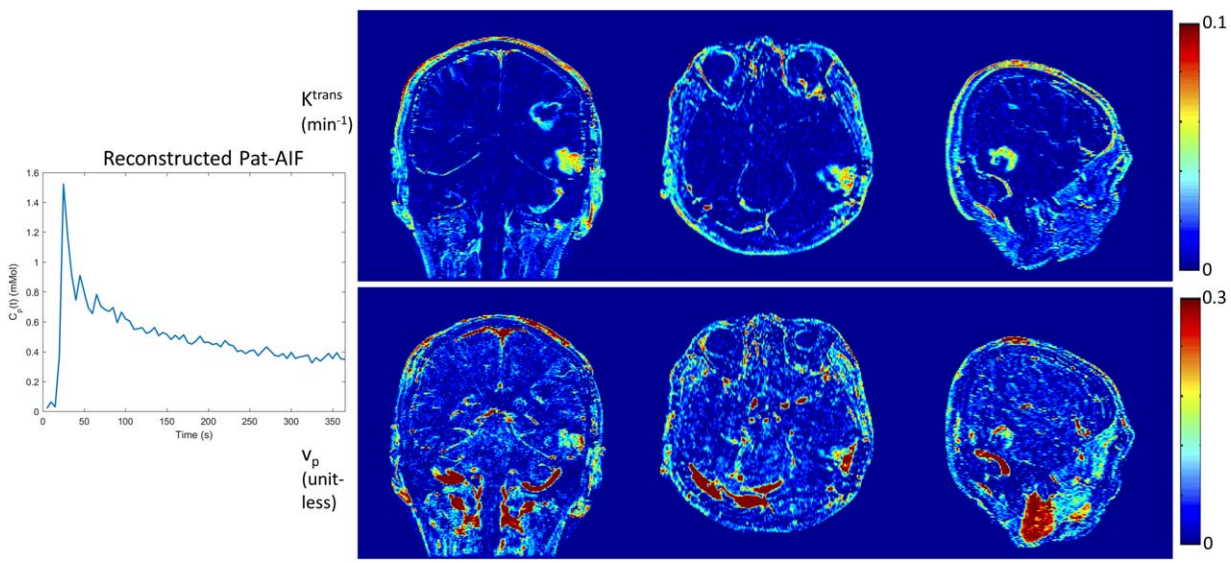

FIG. 10. Joint reconstruction of pat-AIF and TK maps from in vivo prospective undersampled data. Whole-brain high-resolution TK maps can be provided together with pat-AIF using the proposed model-based reconstruction approach.

accumulate during the iteration process. For higher-order TK models, a few linearized approximation approaches have been proposed for fast computation (46,47). Unfortunately, those approximation methods are not compatible with this framework.

Third, although we have shown that this method can include different TK solver, it may be difficult to use a nested model that selects between several different local models based on local fitting errors (23–25). This type of approach has been shown in the literature to be advantageous. The quality of intermediate anatomic images in the proposed method, especially in the first few iterations, may make it challenging to generate a modeling mask needed for nested models.

Fourth, we have not accounted for phase that can be induced by the contrast agent (primarily in vessels). Many centers, including ours, use a half dose for DCE-MRI, which makes this effect negligible. If a full dose is used, the potential phase effects on the AIF signal can and should be modeled using the closed-form solution by Simonis et al. (48).

In conclusion, we have demonstrated a novel model-based reconstruction approach for accelerated DCE-MRI. Posing the TK model as a model consistency constraint, this formulation provides flexible use of different TK solvers, joint estimation of pat-AIF, and straightforward implementation. In anatomically realistic brain tumor DRO studies, the proposed method provides TK maps with low error that are comparable to fully sampled data. In retrospective undersampling studies, this method provides TK maps with nRMSE less than 32% and pat-AIF with nRMSE less than 8% at undersampling rates up to 100×.

ACKNOWLEDGMENTS

We thank Meng Law, Mark S. Shiroshi, Mario Franco, and Samuel Valencerina for help recruiting and scanning brain tumor patients.

APPENDIX

The proposed method uses an alternating approach to solve for C and θ from undersampled k,t-space data. This appendix details the steps involved in solving the two subproblems shown in Equations [3] and [4].

In Equation [3], we solve for the contrast concentration versus time from the measured data using the following equation:

$$C^{n+1} = \underset{C}{\operatorname{argmin}} \, ||AC - b||_2^2 + \beta||P(\theta^n) - C||_2^2, \qquad [3]$$

where $A = UFE\Psi$. We first solve for the image difference (ΔS) from b (since the precontrast signal S_0 is included in b) by solving the following least-square problems using conjugate gradients (or another iterative algorithm for least-square problems). We use the result from the previous iteration as an initial guess for faster convergence:

$$\Delta S = \underset{\Delta S}{\operatorname{argmin}} \, ||UFE(\Delta S) - b||_2^2 + ||\Delta S - \psi P(\theta^n)||_2^2, \qquad [A1]$$

where the first term represents SENSE, and the second term is an identity constraint to $\Psi P(\theta^n)$ that is constant in this step. P is the forward modeling from TK maps to contrast concentration versus time C, and Ψ is the conversion from contrast concentration C to signal difference ΔS following the steady-state SPGR signal equation:

$$\begin{aligned}\Delta S &= \psi(C) \\ &= \frac{M_0 \sin\alpha\left(1 - e^{-TR\cdot(R_0 + C\cdot r_1)}\right)}{1 - \cos\alpha e^{-TR\cdot(R_0 + C\cdot r_1)}} - \frac{M_0 \sin\alpha(1 - e^{-TR\cdot R_0})}{1 - \cos\alpha e^{-TR\cdot R_0}},\end{aligned} \qquad [A2]$$

where TR is the repetition time, α is the flip angle, and r_1 is the contrast agent relaxivity. R_0 and M_0 are the precontrast R_1 (reciprocal of T_1) and the equilibrium longitudinal magnetization that are estimated from a T_1 mapping sequence. In this study, we used DESPOT1 (49) before the DCE-MRI scan.

Note that Ψ is a one-to-one mapping for each voxel, and its inversion [$C = \Psi^{-1}(\Delta S)$] is:

$$\begin{aligned}R_t &= -\frac{1}{TR}\ln\frac{1 - \left(\frac{\Delta S}{M_0\sin\alpha} + \frac{1 - e^{-TR\cdot R_0}}{1 - \cos\alpha e^{-TR\cdot R_0}}\right)}{1 - \cos\alpha\left(\frac{\Delta S}{M_0\sin\alpha} + \frac{1 - e^{-TR\cdot R_0}}{1 - \cos\alpha^{-TR\cdot R_0}}\right)} \\ C &= (R_t - R_0)/r_1\end{aligned} \qquad [A3]$$

Equation [A3] is used to compute C after solving for ΔS using Equation [A1]; this completes the detailed algorithm for solving Equation [3].

After C is estimated, Equation [4] represents backward TK modeling. $C(t)$ is used in the equation below to avoid confusion. For the Patlak model, Equation [4] is expressed as

$$C(t) = P(\theta) = P(K^{trans}, v_p) = K^{trans}\int_0^t C_p(\tau)\,d\tau + v_p C_p(t), \qquad [A4]$$

where $C_p(t)$ is the AIF. The Patlak model is linear, and a pseudo-inverse can be used to solve $\theta = P^{-1}(C)$.

For the eTofts model, Equation [4] is expressed as

$$\begin{aligned}C(t) &= P(\theta) = P(K^{trans}, v_p, K_{ep}) \\ &= K^{trans}\int_0^t C_p(\tau)e^{-K_{ep}(t-\tau)}d\tau + v_p C_p(t),\end{aligned} \qquad [A5]$$

where an extra TK parameter K_{ep} is modeled for better fitting. eTofts is nonlinear, and an iterative algorithm can be used to solve this model fitting:

$$\theta = \underset{\theta}{\operatorname{argmin}} \, ||\, P(\theta) - C\,||_2^2. \qquad [A6]$$

We use a gradient-based l-BFGS algorithm to solve Equation [A6], where we derive the gradient for each TK parameter. In this study, we also used an open-source

DCE-MRI TK modeling toolbox, ROCKETSHIP (31), for comparison.

The code and examples of the proposed algorithm are publicly available at the following URL: https://github.com/usc-mrel/DCE_MOCCO.

REFERENCES

1. Heye AK, Culling RD, Hernández CV, Thrippleton MJ, Wardlaw JM. Assessment of blood–brain barrier disruption using dynamic contrast-enhanced MRI. A systematic review. Neuroimage Clin 2014;6:262–274.
2. Tofts PS, Kermode AG. Measurement of the blood-brain barrier permeability and leakage space using dynamic MR imaging. 1. Fundamental concepts. Magn Reson Med 1991;17:357–367.
3. O'Connor JPB, Jackson A, Parker GJM, Roberts C, Jayson GC. Dynamic contrast-enhanced MRI in clinical trials of antivascular therapies. Nat Rev Clin Oncol 2012;9:167–177.
4. Larsson HB, Stubgaard M, Frederiksen JL, Jensen M, Henriksen O, Paulson OB. Quantitation of blood-brain barrier defect by magnetic resonance imaging and gadolinium-DTPA in patients with multiple sclerosis and brain tumors. Magn Reson Med 1990;16:117–131.
5. Law M, Yang S, Babb JS, et al. Comparison of cerebral blood volume and vascular permeability from dynamic susceptibility contrast-enhanced perfusion MR imaging with glioma grade. Am J Neuroradiol 2004;25:746–755.
6. Montagne A, Barnes SR, Law M, et al. Blood-brain barrier breakdown in the aging human hippocampus. Neuron 2015;85:296–302.
7. Henderson E, Rutt BK, Lee TY. Temporal sampling requirements for the tracer kinetics modeling of breast disease. Magn Reson Imaging 1998;16:1057–1073.
8. Cramer SP, Simonsen H, Frederiksen JL, Rostrup E, Larsson HBW. Abnormal blood-brain barrier permeability in normal appearing white matter in multiple sclerosis investigated by MRI. Neuroimage Clin 2014;4:182–189.
9. Guo Y, Lebel RM, Zhu Y, et al. High-resolution whole-brain DCE-MRI using constrained reconstruction: prospective clinical evaluation in brain tumor patients. Med Phys 2016;43:2013–2023.
10. Feng L, Grimm R, Block KT, et al. Golden-angle radial sparse parallel MRI: combination of compressed sensing, parallel imaging, and golden-angle radial sampling for fast and flexible dynamic volumetric MRI. Magn Reson Med 2014;72:707–717.
11. Lebel RM, Jones J, Ferre J-C, Law M, Nayak KS. Highly accelerated dynamic contrast enhanced imaging. Magn Reson Med 2014;71:635–644.
12. Zhang T, Cheng JY, Potnick AG, et al. Fast pediatric 3D free-breathing abdominal dynamic contrast enhanced MRI with high spatiotemporal resolution. J Magn Reson Imaging 2015;41:460–473.
13. Chandarana H, Feng L, Ream J, et al. Respiratory motion-resolved compressed sensing reconstruction of free-breathing radial acquisition for dynamic liver magnetic resonance imaging. Invest Radiol 2015;50:749–756.
14. Guo Y, Lingala SG, Zhu Y, Lebel RM, Nayak KS. Direct estimation of tracer-kinetic parameter maps from highly undersampled brain dynamic contrast enhanced MRI. Magn Reson Med 2017;78:1566–1578.
15. Sumpf TJ, Uecker M, Boretius S, Frahm J. Model-based nonlinear inverse reconstruction for T2 mapping using highly undersampled spin-echo MRI. J Magn Reson Imaging 2011;34:420–428.
16. Velikina JV, Alexander AL, Samsonov A. Accelerating MR parameter mapping using sparsity-promoting regularization in parametric dimension. Magn Reson Med 2013;70:1263–1273.
17. Lin Y, Haldar J, Li Q, Conti P, Leahy R. Sparsity constrained mixture modeling for the estimation of kinetic parameters in dynamic PET. IEEE Trans Med Imaging 2013;33:173–185.
18. Wang G, Qi J. Direct estimation of kinetic parametric images for dynamic PET. Theranostics 2013:802–815.
19. Dikaios N, Arridge S, Hamy V, Punwani S, Atkinson D. Direct parametric reconstruction from undersampled (k, t)-space data in dynamic contrast enhanced MRI. Med Image Anal 2014;18:989–1001.
20. Felsted BK, Whitaker RT, Schabel M, DiBella EVR. Model-based reconstruction for undersampled dynamic contrast-enhanced MRI. Proc SPIE 2009;7262:1–10.
21. Lingala SG, Guo Y, Zhu Y, Barnes S, Lebel RM, Nayak KS. Accelerated DCE MRI Using Constrained Reconstruction Based on Pharmaco-kinetic Model Dictionaries. In Proceedings of the 23rd Annual Meeting of ISMRM, Toronto, Ontario, Canada, 2015. p. 196.
22. Port RE, Knopp MV, Brix G. Dynamic contrast-enhanced MRI using Gd-DTPA: interindividual variability of the arterial input function and consequences for the assessment of kinetics in tumors. Magn Reson Med 2001;45:1030–1038.
23. Ewing JR, Brown SL, Lu M, et al. Model selection in magnetic resonance imaging measurements of vascular permeability: gadomer in a 9L model of rat cerebral tumor. J Cereb Blood Flow Metab 2006;26:310–320.
24. Bagher-ebadian H, Jain R, Nejad-davarani SP, et al. Model selection for DCE-T1 studies in glioblastoma. Magn Reson Med 2012;68:241–251.
25. Ewing JR, Bagher-Ebadian H. Model selection in measures of vascular parameters using dynamic contrast-enhanced MRI: experimental and clinical applications. NMR Biomed 2013:1028–1041.
26. Shi L, Wang D, Liu W, et al. Automatic detection of arterial input function in dynamic contrast enhanced MRI based on affinity propagation clustering. J Magn Reson Imaging 2014:1327–1337.
27. Parker GJM, Roberts C, Macdonald A, et al. Experimentally-derived functional form for a population-averaged high-temporal-resolution arterial input function for dynamic contrast-enhanced MRI. Magn Reson Med 2006;56:993–1000.
28. Samsonov A. A Novel Reconstruction Approach Using Model Consistency Condition for Accelerated Quantitative MRI (MOCCA). In Proceedings of the 20th Annual Meeting of ISMRM, Melbourne, Victoria, Australia, 2012. p. 358.
29. Velikina JV, Samsonov AA. Reconstruction of dynamic image series from undersampled MRI data using data-driven model consistency condition (MOCCO). Magn Reson Med 2015;74:1279–1290.
30. Pruessmann KP, Weiger M, Börnert P, Boesiger P. Advances in sensitivity encoding with arbitrary k-space trajectories. Magn Reson Med 2001;46:638–651.
31. Barnes SR, Ng TSC, Santa-Maria N, Montagne A, Zlokovic BV, Jacobs RE. ROCKETSHIP: a flexible and modular software tool for the planning, processing and analysis of dynamic MRI studies. BMC Med Imaging 2015;15:19.
32. Barboriak DP, MacFall JR, Padua AO, York GE, Viglianti BL and MWD. Standardized Software for Calculation of Ktrans and vp from Dynamic T1-Weighted MR Images. Presented at the ISMRM Workshop on MR in Drug Development: From Discovery to Clinical Therapeutic Trials, McLean, Virginia, USA, April 2004.
33. Dikaios N, Punwani S, Atkinson D. Direct Parametric Reconstruction from (k, t)-Space Data in Dynamic Contrast Enhanced MRI. In Proceedings of the 23rd Annual Meeting of ISMRM, Toronto, Ontario, Canada, 2015. p. 3706.
34. Bosca RJ, Jackson EF. Creating an anthropomorphic digital MR phantom—an extensible tool for comparing and evaluating quantitative imaging algorithms. Phys Med Biol 2016;61:974–982.
35. Zhu Y, Guo Y, Lingala SG, et al. Evaluation of DCE-MRI Data Ssampling, Reconstruction and Model Fitting Using Digital Brain Phantom. In Proceedings of the 23rd Annual Meeting of ISMRM, Toronto, Ontario, Canada, 2015. p. 3070.
36. Stanisz GJ, Henkelman RM. Gd-DTPA relaxivity depends on macromolecular content. Magn Reson Med 2000;44:665–667.
37. Zhu Y, Guo Y, Lingala SG, Lebel RM, Law M, Nayak KS. GOCART: GOlden-angle CArtesian randomized time-resolved 3D MRI. Magn Reson Imaging 2016;34:940–950.
38. Thomas AA, Arevalo-Perez J, Kaley T, et al. Dynamic contrast enhanced T1 MRI perfusion differentiates pseudoprogression from recurrent glioblastoma. J Neurooncol 2015;125:183–190.
39. Jung SC, Yeom JA, Kim J, et al. Glioma: application of histogram analysis of pharmacokinetic parameters from T1-weighted dynamic contrast-enhanced MR imaging to tumor grading. AJNR Am J Neuroradiol 2014:1103–1110.
40. Markowski CA, Markowski EP. Conditions for the effectiveness of a preliminary test of variance. Am Stat 1990;44:322–326.
41. Anderson KB, Conder JA. Discussion of multicyclic Hubbert modeling as a method for forecasting future petroleum production. Energy Fuels 2011;25:1578–1584.
42. Lebel RM, Guo Y, Zhu Y, et al. The Comprehensive Contrast-Enhanced Neuro Exam. In Proceedings of the 23rd Annual Meeting of ISMRM, Toronto, Ontario, Canada, 2015. p. 3705.

43. Baek HJ, Kim HS, Kim N, Choi YJ, Kim YJ. Percent change of perfusion skewness and kurtosis: a potential imaging biomarker for early treatment response in patients with newly diagnosed glioblastomas. Radiology 2012;264:834–843.
44. Guo Y, Lebel RM, Zhu Y, et al. High-Resolution Whole-Brain DCE-MRI Using constrained reconstruction: prospective clinical evaluation in brain tumor patients. Med Phys 2016;43:2013.
45. Bertsekas DP. Multiplier methods: a survey. Automatica 1976;12:133–145.
46. Murase K. Efficient method for calculating kinetic parameters using T1-weighted dynamic contrast-enhanced magnetic resonance imaging. Magn Reson Med 2004;51:858–862.
47. Flouri D, Lesnic D, Sourbron SP. Fitting the two-compartment model in DCE-MRI by linear inversion. Magn Reson Med 2016;76:998–1006.
48. Simonis FF, Sbrizzi A, Beld E, Lagendijk JJ, van den Berg CA. Improving the arterial input function in dynamic contrast enhanced MRI by fitting the signal in the complex plane. Magn Reson Med 2016;76:1236–1245.
49. Deoni SCL, Peters TM, Rutt BK. High-resolution T1 and T2 mapping of the brain in a clinically acceptable time with DESPOT1 and DESPOT2. Magn Reson Med 2005;53:237–241.

SUPPORTING INFORMATION

Additional Supporting Information may be found in the online version of this article.

Video S1. Movie of estimated pat-AIF versus iteration number at undersampling rate R = 20×, 40×, 60×, 80×, 100×, 120×.